Computers & Fluids 88 (2013) 354–362

Contents lists available at ScienceDirect

Computers & Fluids

journal homepage: www.elsevier.com/locate/compfluid

An exact solution of interception efficiency over a circular-arc fiber collector

Mingliang Xie [a], Qing He [a], Wenxi Wang [b,*], Lian-Ping Wang [a,c]

[a] State Key Laboratory of Coal Combustion, Huazhong University of Science and Technology, Wuhan 430074, China
[b] Henan Electric Power Survey & Design Institute, Zhengzhou 450007, China
[c] Department of Mechanical Engineering, University of Delaware, Newark, DE 19716, USA

ARTICLE INFO

Article history:
Received 27 June 2013
Received in revised form 10 September 2013
Accepted 23 September 2013
Available online 2 October 2013

Keywords:
Inviscid flow
Potential equation
Zhukovsky conversion
Interception efficiency
Arc fiber

ABSTRACT

In this paper, an exact solution is developed to predict the single-fiber interception efficiency of spherical particles carried by a potential flow over a circular-arc fibrous filter. The flow field around the arc fiber has recently been calculated based on the Zhukovsky conversion. It is shown that the interception efficiency is a function of three parameters: the arc shape parameter, the flow-approaching angle, and the particle size. The results show that slim and long arc fibers have higher interception efficiency. The interception efficiency increases as the particle diameter increases. The orientation angle also affects the interception efficiency. Overall, the results demonstrate the importance of flow asymmetry and singular points on the interception efficiency. Together with our previous results on elliptic fibers published in Wang et al. [Wang WX, Xie ML, Wang LP. An exact solution of interception efficiency over an elliptical fiber collector. Aerosol Sci Technol 2012;46:843–51.], a range of fiber cross-sectional shapes on the interception efficiency can now be analytically modeled.

1. Introduction

Fibrous filters are ubiquitous in nature and in engineered systems. They form the heart of many filtration and particle-separation devices in environmental, electrical, biological and chemical engineering applications. Examples of their use include respiratory protection, control of diesel particle emissions, and air cleaning equipment.

A key characteristic of filters is the filtration efficiency, which has attracted a great deal of interest. The two major theoretical difficulties that have long been recognized are the treatment of the interference effects of neighboring fibers and the consideration of effects associated with arbitrary fiber orientation. There have been extensive theoretical and experimental investigations addressing these issues of filtration mechanisms [10]. Lee and Liu studied the filtration efficiency of aerosols by fibrous filters both theoretically [8] and experimentally [9]. Considering the influences of neighboring fibers, their theoretical and experimental results were fairly consistent, that is, diffusion and interception play a major role in the region of minimum efficiency while impaction with minor effect. Fotovati et al. [4] and Tahir and Tafreshi [14] respectively investigated the influence of fiber orientation on the performance of fibrous filters. They both found that capture efficiencies of submicron particles by common fibrous filters were independent of in-plane fiber orientation but decreased as the fibers' through-plane angle increased from the zero reference value.

As changing some of the filter parameters is usually accompanied by an increase in pressure drop across the filter, some researchers paid attention to the application of external fields, such as electrostatic, magnetic or acoustic, which might enhance the filtration efficiency without a change in pressure drop. Moldavsky et al. [11] have investigated the influence of acoustic waves on the performance of fibrous filters; Wang [17] found that application of electrostatic forces could significantly increase the efficiency for removing sub-micrometer particles from a gas stream; Watson [22] investigated the filtering process of removing micron-sized paramagnetic particles from a fluid and considered application of magnetic filtering to the rapid treatment of sewage.

Theoretically, in order to reduce the many complications of a filtering process, "single fiber theory" is used instead to predict the filter efficiency. The single-fiber filtration efficiency serves as a key parameter to describe the filtration behavior of unloaded fibrous filters. It is mainly determined by 3 mechanisms: (1) impaction; (2) direct interception; and (3) diffusion according to the classic filtration theory [5]. Diffusion is the dominant deposition mechanism for nanoparticle filtration while interception and inertial impaction play a major role for particles larger than

* Corresponding author. Tel.: +86 13277040393.
E-mail address: 10408045@zju.edu.cn (W. Wang).

0045-7930/$ - see front matter © 2013 Elsevier Ltd. All rights reserved.
http://dx.doi.org/10.1016/j.compfluid.2013.09.025

Nomenclature

A/B	the right/left tangent point of the circular-arc
b	the chord half width of the circular-arc
C/D	the center point of right/left particles with diameter d_p just passing the circular-arc
f_1	the height of the circular-arc
R	the circular-arc radius
L	the distance of two parallel lines of same orientation that are tangential to the fiber
L_i	the line pass through point ($x_{i\infty}$,$y_{i\infty}$) with the orientation angle α
L_∞	the distance between the two limiting streamlines along which particles would just touch the fiber from above and below
K	the intercept
V	the velocity of incoming flow
x	the horizontal axis on circular-arc plane
x'	x-coordinate of point A
x_0	x-coordinate of point B
x_1	x-coordinate of point C
x_2	x-coordinate of point D
$x_{i\infty}$	x-coordinate of point located at the streamline at the infinity
y	the vertical axis on circular-arc plane
y'	y-coordinate of point A
y_0	y-coordinate of point B
y_1	y-coordinate of point C
y_2	y-coordinate of point D
$y_{i\infty}$	y-coordinate of point located at the streamline at the infinity
z	a vector on circular-arc plane
α	the orientation angle of incoming flow
θ	the half angle of the circular-arc
ζ	the transformed vector on circular plane from z
ξ	the horizontal axis on circular plane
η	the vertical axis on circular plane
Ψ	the stream function

500 nm at normal temperatures and pressures [1]. It is typically derived under the assumptions that the particles are spherical and do not bounce once touch the fiber. There are many studies addressing the thermal rebound due to the particles' high thermal speed, which considered occurring for particles smaller than 2 nm (e.g. [19]; and [6]. In addition, the change of the particles' shape and size, such as due to Brownian coagulation [23], straining and some other physical and chemical processes, could also affect the porous filter efficiency. For example, the straining of particles makes the filtration coefficients not proportional to the fractional flow through the pores smaller than the particles, but to the power-law functions of them [24]. Yuan et al. [25] also provide a new improved population balance methodology for modeling of the straining-dominant deep bed filtration in porous filters.

Most of the existing theory for filtration of aerosols by fibrous media assumes that the fibers have circular cross-sections. As the noncircular fibers can offer more surface per unit volume of fiber than circular fibers and with the development of technology, many other studies are focused on the noncircular cross-sectional shapes, including ellipse [20], square or rectangular [2,3,12], as well as "+" shaped, "T" shaped, "O" hollow shaped [15]. In this study we consider analytically the case of a circular-arc fiber, which to our knowledge has never been dealt with previously. Obviously, a circular-arc fiber has a larger specific surface area than a circular fiber, which leads to more absorption area under the same conditions. When the arc angle tends to 2π, the arc are close to a hollow cylinder in which case it may offer a similar filter efficiency compared to the cylindrical one with less cost of material and simple technology. We first discuss the potential flow around a circular-arc fiber assuming that the Reynolds number is high enough. Usually the viscous force is negligible to the inertial force when Re $\geqslant$ 1000 in which situation the potential flow assumption is available. And in Viswanathan [16], it shows that the transition from intermediate to potential flow occurs when the Reynolds number is about 80. Furthermore, the Reynolds number is usually high for particle-laden flow, so that some researchers paid attention to the deposition of aerosol particles at high Reynolds number [18,13]. All these make the applications of potential flow possible although the predicted interception efficiency may be somewhat overestimated. Based on the theory of Zhukovsky conversion [7], a potential flow field around a circular-arc fiber can be obtained [21]. When the degree of filter loading and external forces are neglected, an exact expression is derived for calculating the single fiber interception efficiency of a particle over the circular-arc fiber collector. The interception efficiency is a function of several variables, including size of the filter elements, diameter of the particle and the orientation angle of the incoming flow.

2. Theory and solution method

In this paper, only the interception efficiency will be considered. Interception efficiency is the theoretical collection efficiency by a fiber for spherical particles under the assumption that both the particle inertia relative to the flow and the Brownian diffusion are negligible so that they follow air streamlines around the fiber.

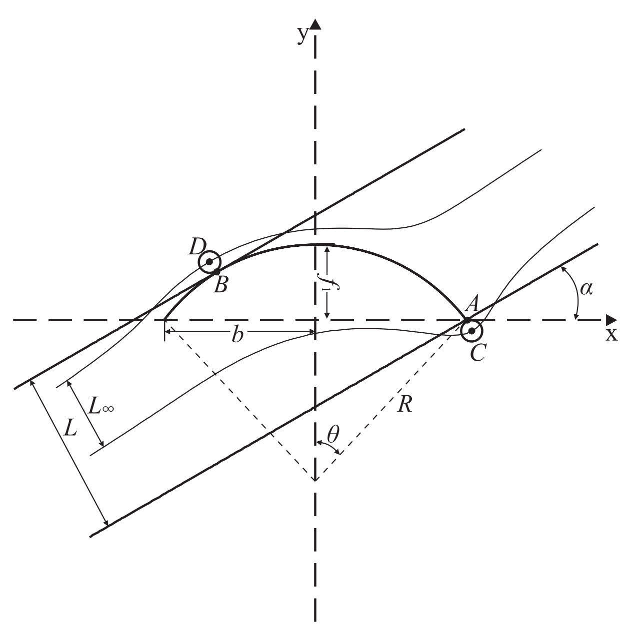

Fig. 1. The sketch of potential flow passing through a circular arc and terminology used to describe the circular arc fiber.

If the center of a particle passes within one particle radius from the surface of a fiber, the particle is considered having been collected by the fiber. Therefore, the interception efficiency is given as:

$$\eta_R = \frac{L_\infty}{L}. \tag{1}$$

where L_∞ is the distance between the two limiting streamlines along which particles would just touch the fiber from above and below, respectively (Fig. 1). The surface contact points are denoted by A and B, respectively, for the two limiting streamlines. In the far field, these two limiting streamlines are parallel to one another with a slope of $\tan\alpha$, where α denotes the orientation of the far field flow. For convenience and without the loss of generality, the range of α in this study is limited from 0 to $\pi/2$ (or 0–90°). L is the distance of two parallel lines of same orientation that are tangential to the fiber. To bound η_R to within unity, we add the particle diameter to the denominator, and the corresponding interception efficiency becomes,

$$\eta_R = \frac{L_\infty}{L + d_p}. \tag{2}$$

The two definitions (Eq. (1)) and (Eq. (2)) yield a similar result only when $d_p \ll L$.

Consider a potential flow around a circular arc as shown in Fig. 1. A circular arc is a portion of a circle being cut off at the chord line. The arc has a radius R and angle (2θ). The chord is aligned with the x-axis. The chord half width is b and the height of the arc is f_1. The left tip and right tip are the two points shared by the arc and the chord. Clearly, the following relationship holds

$$b = R\sin\theta; \quad f_1 = R(1-\cos\theta). \tag{3}$$

It follows that the arc radius R and the arc half angle θ can be determined from the chord half width b and the height f_1 as

$$R = \frac{b^2 + f_1^2}{2f_1}, \tag{4}$$

$$\theta = \cos^{-1}\left[1 - \left(\frac{f_1}{b}\right)^2\right] \Big/ \left[1 + \left(\frac{f_1}{b}\right)^2\right]. \tag{5}$$

Therefore, a give value of (f_1/b) in the range $0 \leqslant f_1/b \leqslant \infty$ corresponds to a unique arc half-angle θ $(0 \leqslant \theta \leqslant \pi)$, as illustrated in Fig. 2a. The relationship is monotonic: increasing (f_1/b) leads to increasing θ. There are three possible relationships between α and f_1/b according to the value f_1/b as shown in Fig. 2b.

It is important to recognize the locations of the contact points A and B (see Fig. 1), relative to the right and left tip of the circular arc. For this purpose, we need to consider three possible configurations as illustrated in Fig. 3. When $\theta \leqslant \pi/2$, two possible configurations could occur. In configuration (a), the contact points are exactly the tip points: this occurs when $\theta \leqslant \alpha \leqslant \pi/2$ or equivalently when $f_1/b \leqslant (1-\cos\alpha)/\sin\alpha \leqslant 1$. Otherwise when $0 \leqslant \alpha < \theta$ or equivalently when $0 \leqslant (1-\cos\alpha)/\sin\alpha \leqslant f_1/b$, the contact point A remains as the right tip but the contact point B appears on the arc; this is configuration (b) shown in Fig. 3. When $\theta > \pi/2$, again two possible configurations could occur. Configuration (b) takes place when $0 \leqslant \alpha \leqslant \pi - \theta$ or equivalently when $f_1/b \leqslant (1+\cos\alpha)/\sin\alpha < \infty$. A third configuration, configuration (c), occurs when $\pi - \theta \leqslant \alpha \leqslant \pi/2$ or $1 \leqslant (1+\cos\alpha)/\sin\alpha < f_1/b$: in this case, both contact points are located on the arc (Fig. 3c).

The determination of L_∞ requires a potential flow solution around the circular arc, which has recently been obtained analytically by Wang et al. [21]. Through the use of the following Zhukovsky conversion $\zeta = \zeta(\xi,\eta) \Leftrightarrow z = z(x,y)$

$$\zeta = z + \sqrt{z^2 - b^2}. \tag{6}$$

Under this transformation, a shifted circle in the transformed plane

$$|\zeta - f_1 i| = \sqrt{f_1^2 + b^2}. \tag{7}$$

corresponds to, in the $z = (x,y)$ plane, an arc of chord width $(2b)$ and height f_1, namely,

$$x^2 + [y + (R - f_1)]^2 = R^2 \qquad \text{with} \qquad y \geqslant 0. \tag{8}$$

Fig. 4 shows how the normalized arc radius (R/b) and arc half angle θ change with the ratio f_1/b. For a fixed b, the arc half angle θ changes from 0 to π as f_1/b is increased from 0 to ∞ (Fig. 4). The normalized arc radius (R/b) approaches infinity for the two limits $f_1/b \to 0$ and $f_1/b \to \infty$ where the arc reduces simply to a straight line of width $2b$ $(f_1/b \to 0)$ or a circle with radius $R \to 1/2\, f_1$ $(f_1/b \to \infty)$. The normalized arc radius (R/b) reaches a minimum value of one when $f_1/b = 1$, in this case the arc covers exactly half of a circle.

The stream-function can be expressed analytically as [21]

$$\frac{\psi}{bV_\infty} = \frac{1}{2}\left[\left(\frac{\eta}{b} - \frac{f_1}{b}\right)\cos\alpha - \frac{\xi}{b}\sin\alpha\right]\left[1 - \frac{1 + \left(\frac{f_1}{b}\right)^2}{\left(\frac{\xi}{b}\right)^2 + \left(\frac{\eta}{b} - \frac{f_1}{b}\right)^2}\right]. \tag{9}$$

where the correct transformation from (x,y) to (ξ,η) requires a careful selection of sign combination in the following relationships

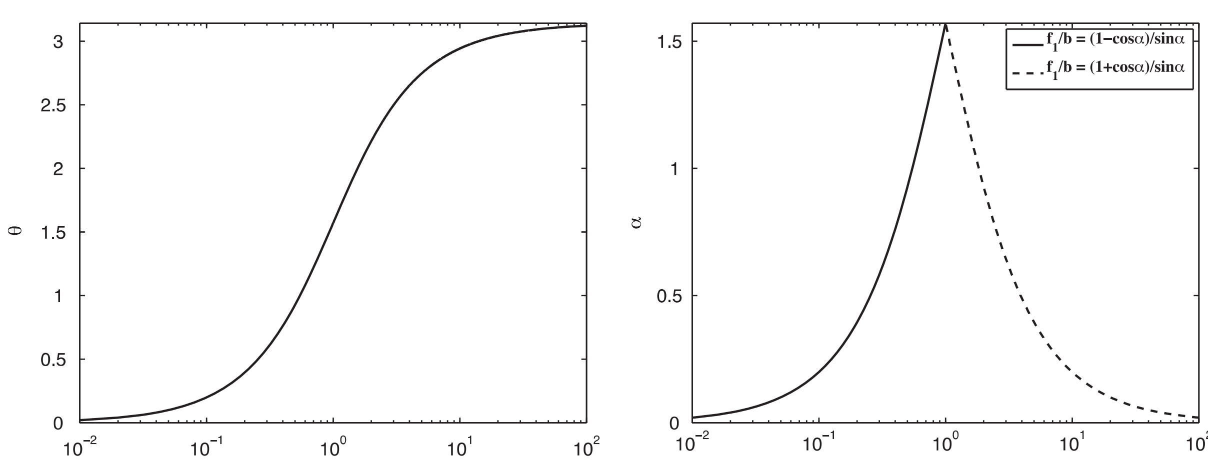

Fig. 2. Configuration map: (a) relationship between θ and (f_1/b) and (b) relationship between α and (f_1/b) at the boundary of three configurations. Note that each (f_1/b) value corresponds to a particular arc half angle θ; the boundaries for the three configurations are shown as the lines $f_1/b = (1-\cos\alpha)/\sin\alpha$ and $f_1/b = (1+\cos\alpha)/\sin\alpha$.

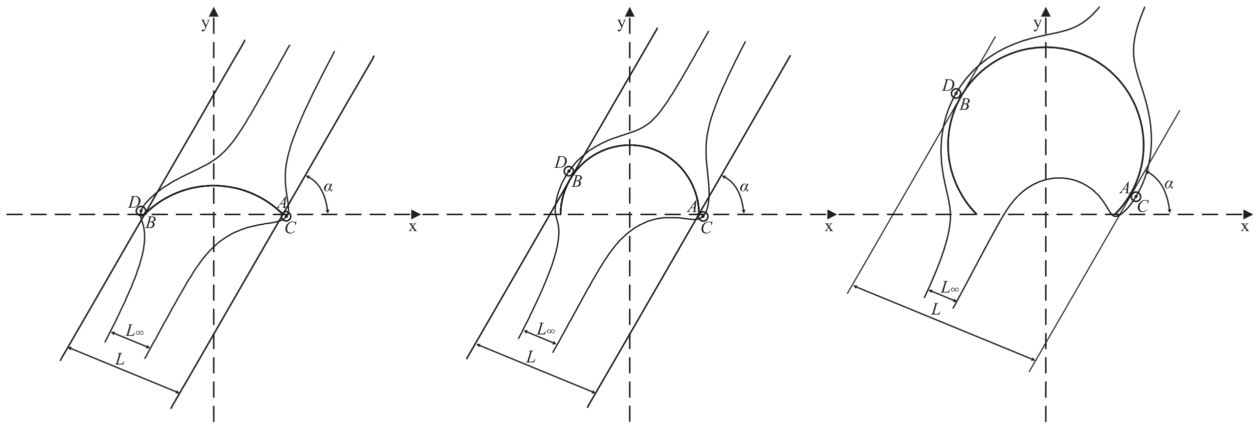

Fig. 3. Three possible configurations of the limiting streamlines: (a) the contact point A coincide with the right tip and B with the left tip: $\theta \leqslant \pi/2$ and $\theta \leqslant \alpha \leqslant \pi/2$ [or equivalently $f_1/b \leqslant (1-\cos\alpha)/\sin\alpha \leqslant 1$]; (b) the contact point B sits on the arc but the contact point A coincides with the right tip: $\theta \leqslant \pi/2$ and $0 \leqslant \alpha < \theta$, or $\theta > \pi/2$ and $0 \leqslant \alpha \leqslant \pi - \theta$; and (c) both contact points A and B are located on the arc: $\theta > \pi/2$ and $\pi - \theta \leqslant \alpha \leqslant \pi/2$ [or equivalently $1 \leqslant (1+\cos\alpha)/\sin\alpha < f_1/b$].

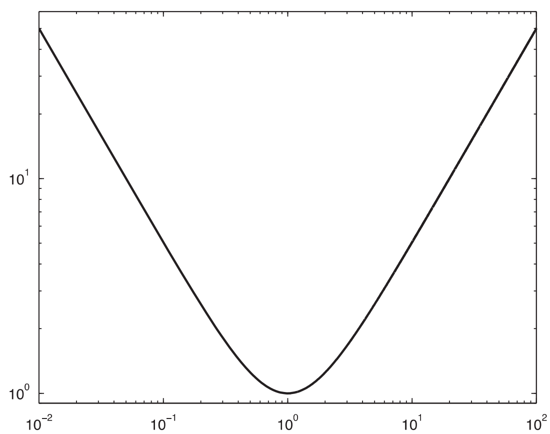

Fig. 4. The normalized arc radius (R/b) as a function of (f_1/b).

$$\xi = x \pm \sqrt{\frac{\sqrt{\left(x^2-y^2-b^2\right)^2+4x^2y^2}+(x^2-y^2-b^2)}{2}},$$
$$\eta = y \pm \sqrt{\frac{\sqrt{\left(x^2-y^2-b^2\right)^2+4x^2y^2}-(x^2-y^2-b^2)}{2}}. \tag{10}$$

In the study [21] the choice of sign is consistent with that of x(or y). But there may exist some questions. In this paper, we provide another possibility, which looks like more reasonable in practice.

There are 6 distinct subdomains with each having a unique sign combination, as shown in Fig. 5. For example, in subdomain V shown in Fig. 5, the "+" sign should be used in the ξ expression, and the "−" sign should be used in the η expression. This proper mapping of sign combinations is crucial for correctly realizing the stream function in the (x,y) space. The mapping shown in Fig. 5 is obtained by first converting the arc in the (x,y) plane to the circle in the (ξ,η). The body must be divided into 4 segments: arc $4 \to 1$, arc $1 \to 3$, arc $3 \to 2$, and arc $2 \to 4$. The first two arcs form the upper branch of the circle and the last two the lower branch in the (ξ,η) plane. In the plane, the lower and upper branches overlap precisely. The mapping of the body surface led to the conclusion that the arcs $4 \to 1$, arc $1 \to 3$, arc $3 \to 2$, and arc $2 \to 4$ are properly transformed with the following sign combinations, (+,+), (−,+), (+,−) and (−,−), respectively. Next, we identify the boundary for each subdomain. The requirement on the boundary is that both variables (ξ,η) must be continuous across a boundary, although the sign may change. Take, for example, the boundary $1 \to 10$ between subdomain I and subdomain II. Across this line, η_+ is used and $\xi_+ = \xi_- = 0$, so there is no problem of using ξ_- on the left of the line and ξ_+ on the right of the line. Here ξ_- denotes the ξ expression with the use of "−" sign. An important

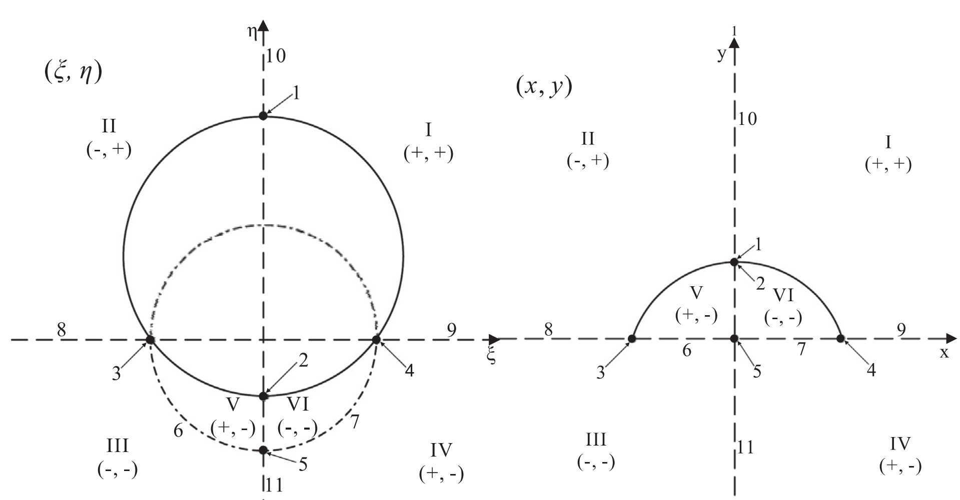

Fig. 5. Sketches to show one-to-one mapping and choices of signs for (x,y) to (ξ,η). Transformation in Eqs. (10). The flow region has to be divided into six subdomains and in each subdomain the proper signs to be used in the transformation are indicated.

next step is to recognize that the subdomains V and VI are both bounded. The portions of the boundaries, $3 \to 6 \to 5$ and $5 \to 7 \to 4$, are on a circle $\xi^2 + \eta^2 = b^2$ in the (ξ, η) plane. Finally, the two additional subdomains III and IV are needed to match the proper far-field conditions. About 11 key points are marked in Fig. 5 to clearly show the one-to-one mapping.

Fig. 6 shows streamlines for three representative cases. In all cases, the streamlines are smooth although six subdomains as shown in Fig. 5 must be identified when computing the stream function. No flow separation is observed. In configuration (a), in addition to the two tip points, two stagnation points are visible, one below the arc and a second above the arc. In configuration (b), both stagnation points are located above the arc. Finally, in configuration (c), there appears to be a significant region below the arc where the flow velocity is essentially zero. The two tip points represent singular points where the local velocity gradient is unbounded.

Now the task is to find the two limiting streamlines that pass through point C (x_1, y_1) and point D (x_2, y_2), respectively. The coordinate locations for points C and D are given by

$$x_1 = x' + \frac{d_p}{2}\sin\alpha, \quad y_1 = y' - \frac{d_p}{2}\cos\alpha. \tag{11}$$

and

$$x_2 = x_0 - \frac{d_p}{2}\sin\alpha, \quad y_2 = y_0 + \frac{d_p}{2}\cos\alpha. \tag{12}$$

Since in the far field ($|x|/b \gg 1$, $|y|/b \gg 1$), the stream-function takes the form

$$\psi \to V_\infty(-x\sin\alpha + y\cos\alpha) + \text{constant}. \tag{13}$$

It follows that, formally, we can express

$$\frac{L_\infty}{b} = \frac{1}{bV_\infty}\mid \psi(x_1, y_1) - \psi(x_2, y_2) \mid . \tag{14}$$

At this point, the task of determining L_∞/b and L/b reduces to the determination of the coordinates for the two contact points A (x', y') and B (x_0, y_0). Both L_∞/b and L/b are functions of three system parameters: α, f_1/b and d_p/b, and they are independent of V_∞. The details are presented in Appendix A according to the solution, Eq. (9) for the three possible configurations illustrated in Fig. 3. Therefore, the interception efficiency depends on the three parameters as

$$\eta_R = \frac{L_\infty}{L + d_p} = f\left(\alpha, \frac{f_1}{b}, \frac{d_p}{b}\right). \tag{15}$$

3. Results and discussion

We shall now present results for the interception efficiency η_R for various combination of the parameters α, f_1/b and d_p/b.

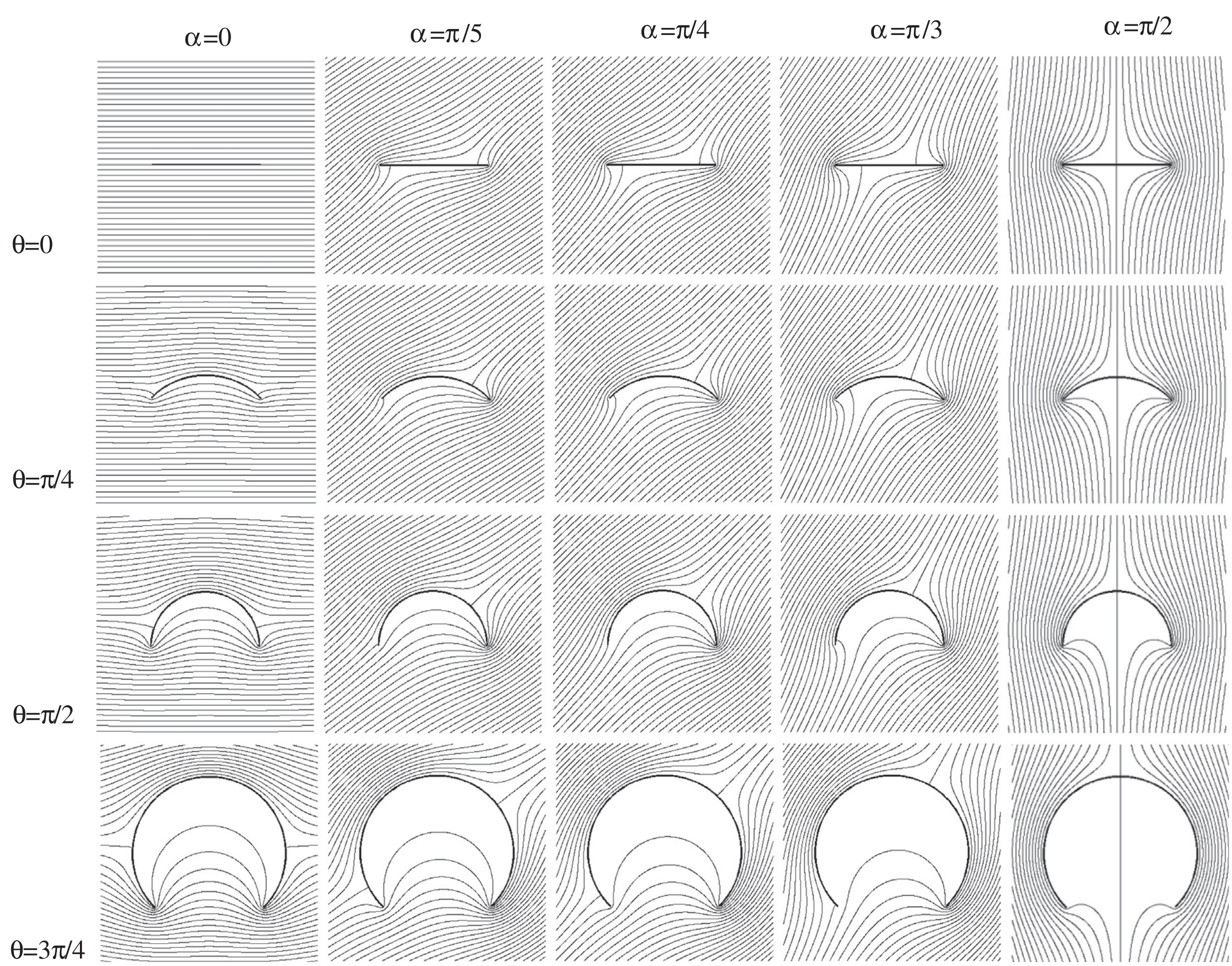

Fig. 6. Streamlines for the representatives flow configurations. All plots represent contours of Ψ/bV_∞, the contour interval is set to 0.1. The arc fiber is indicated by the bold black line and the arc half width $b = 1$.

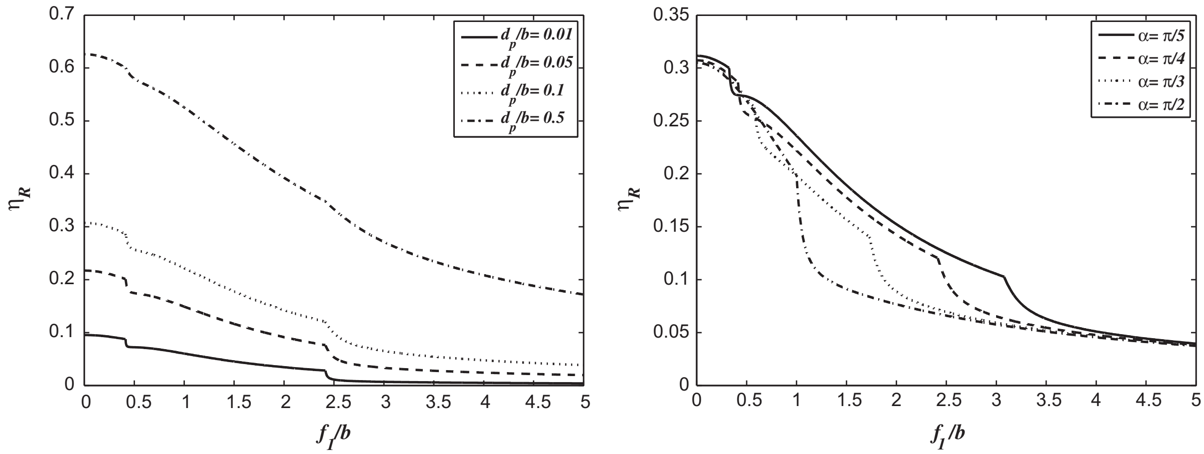

Fig. 7. The effect of arc shape parameter f_1/b on the interception efficiency, (a) different d_p/b values at a fixed flow approaching angle $\alpha = \pi/4$ and (b) different flow approaching angles at given particle size $d_p/b = 0.1$.

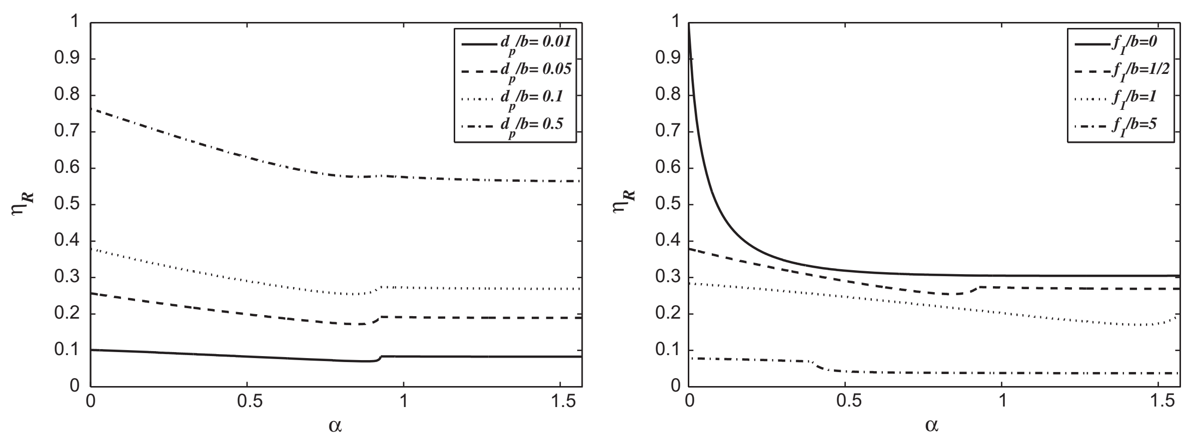

Fig. 8. The effect of orientation angle of incoming flow on the interception efficiency, (a) different d_p/b at $f_1/b = 1/2$ and (b) different f_1/b at $d_p/b = 0.1$.

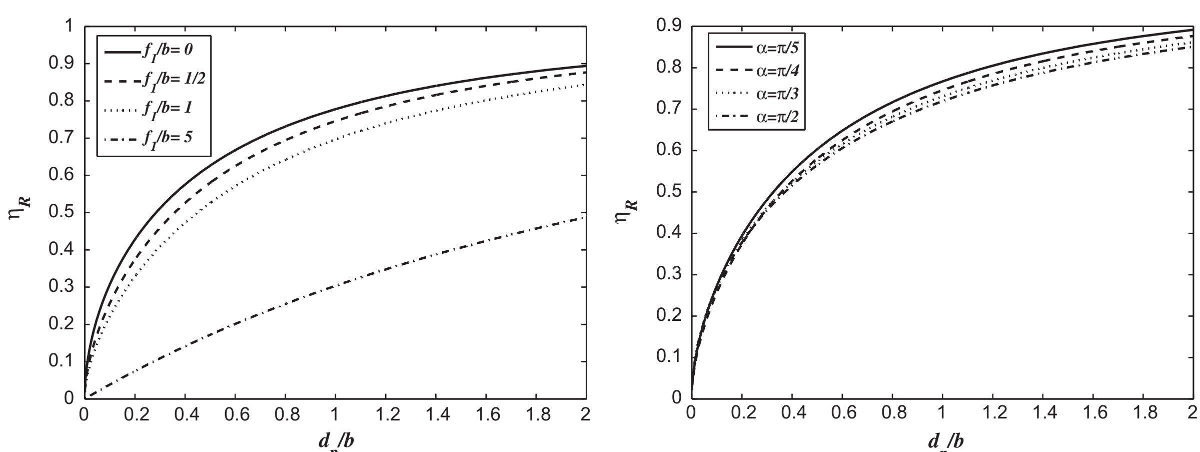

Fig. 9. The effect of particle size d_p on the interception efficiency: (a) different f_1/b at $\alpha = \pi/4$ and (b) different α at $f_1/b = 1/2$.

3.1. The effect of the arc shape parameter f_1/b

We first consider the dependence of interception efficiency on the arc shape parameter. A small value of f_1/b represents a line object, while a large f_1/b represents a more round arc fiber. In Fig. 2 we observe that η_R decreases as the ratio f_1/b increases, this shows that the more slim the arc is, the higher the interception efficiency it has. Fig. 2(a) shows that the arc filter works better for relatively larger particles due to the strong converging–diverging streamlines at the tips. Fig. 7(b) shows that the interception efficiency is higher for a smaller approaching angle, perhaps due to the asymmetry of the flow streamlines. This dependence, however, is weak for very slim and very round arcs. For a large f_1/b, the arc is close to a circle, and η_R should be independent of the orientation angle.

3.2. The effect of the orientation angle of incoming flow (α)

In Fig. 8, we study how the interception efficiency changes with the flow-approaching angle α. In general we observe that η_R decreases with increasing α in the range of 0–$\pi/2$, but becomes almost independent of α when α tends to $\pi/2$. η_R is higher if the diameter of the particle is larger or f_1/b is smaller. The maximum interception efficiency is located at $\alpha = 0$ with a fixed d_p/b and f_1/b. Since the maximum blocking L is very small for small α, the net collection rate for small α is likely to be insignificant.

3.3. The effect of particle size d_p

Finally, in Fig. 9 we show the dependence of η_R in the particle size d_p/b, for different f_1/b or α values. Clearly, d_p/b, relative to the other two parameters, has the strongest impact on the interception efficiency due to the strong flow singularity at the tips. At a given d_p/b, a slim arc or a smaller orientation angle yields higher interception efficiency due to flow asymmetry. For very small particles, the interception efficiency is close to zero regardless the fiber shape and orientation angle. The effect of the arc shape is stronger for larger particles.

4. Conclusion

In this study, an exact solution for the single-fiber interception efficiency of spherical particles carried by a potential flow over a circular-arc fiber has been developed. The potential flow field around the arc fiber has recently been calculated based on the Zhukovsky conversion by Wang et al. [21]. The interception efficiency has been shown to depend on three parameters: the arc shape parameter, the flow-approaching angle, and the particle size. The results show that the slim and long arc plate has higher interception efficiency. When the arc is close to a circle, the interception efficiency approaches a limited value independent of the flow orientation angle. With a given size of the filter element and particle diameter, the maximum interception efficiency occurs when the incoming flow is parallel to the chord of the arc. However, in this case, the cross-sectional projection area is at a minimum, therefore, the net collection rate is not significant. The interception efficiency depends strongly on the particle size due to the singular flow streamlines near the arc tips. For large particles, both the interception and inertial impaction mechanisms play a major role during filtration processes.

While this study addressed a special case of circular arc fiber, the results are also indicative of circular segment fibers (namely, fibers with a cross section bounded by the arc on top and the chord at bottom). Overall, the results indicate the importance of flow asymmetry and fiber corner points (arc tips) on the interception efficiency. Together with previous results on elliptic fibers[12] and other shapes, a range of fiber cross-sectional shapes on the interception efficiency can now be analytically modeled.

Acknowledgements

This work is supported by the National Natural Science Foundation of China with Grant No. 50806023, and the National Natural Science Foundation of China with Grant No. 50721005, and the Fundamental Research Funds for Central Universities with Grant No. 2013TS078, and the Programmer of Introducing Talents of Discipline to Universities ("111" Project No. B06019), China.

Appendix A. Determination of L_∞/b and L/b

As explained in the section *Theory and Solution Method*, there are three possible configurations of the limiting streamlines depending on the magnitudes of θ (or f_1/b) and α. We shall consider each case separately. The key is the proper determination of coordinates for A, B, C, and D. We will first give explicit expressions for L/b, and then formulation the expression for L_∞/b.

A.1. Configuration (a): $\theta \leqslant \pi/2$ and $\theta \leqslant \alpha \leqslant \pi/2$ [or equivalently $f_1/b \leqslant (1-\cos\alpha)/\sin\alpha \leqslant 1$]

In this case, the tangent contact points A and B are the right and left tip, respectively. Therefore,

$$\begin{aligned} x_1 &= b + \tfrac{d_p}{2}\sin\alpha, \\ y_1 &= -\tfrac{d_p}{2}\cos\alpha, \end{aligned} \tag{A1}$$

$$\begin{aligned} x_2 &= -b - \tfrac{d_p}{2}\sin\alpha, \\ y_2 &= \tfrac{d_p}{2}\cos\alpha. \end{aligned} \tag{A2}$$

We obtain

$$\frac{L}{b} = \frac{2\tan\alpha}{\sqrt{1+\tan^2\alpha}} = 2\sin\alpha. \tag{A3}$$

A.2. Configuration (b): $\theta \leqslant \pi/2$ and $0 \leqslant \alpha < \theta$, or $\theta > \pi/2$ and $0 \leqslant \alpha \leqslant \pi-\theta$ [$(1-\cos\alpha)/\sin\alpha < f_1/b \leqslant (1+\cos\alpha)/\sin\alpha$]

In this second case, the tangent contact points A and B are specified as

$$\begin{aligned} x' &= b, \\ y' &= 0, \end{aligned} \tag{A4}$$

$$\begin{aligned} x_0 &= -\tfrac{1}{2}\left(\tfrac{b^2}{f_1}+f_1\right)\sin\alpha, \\ y_0 &= \tfrac{1}{2}\left(\tfrac{b^2}{f_1}+f_1\right)\cos\alpha - \tfrac{1}{2}\left(\tfrac{b^2}{f_1}-f_1\right). \end{aligned} \tag{A5}$$

It follows that the two limiting streamlines must pass the following points, respectively,

$$\begin{aligned} x_1 &= b + \tfrac{d_p}{2}\sin\alpha, \\ y_1 &= -\tfrac{d_p}{2}\cos\alpha, \end{aligned} \tag{A6}$$

$$\begin{aligned} x_2 &= -\tfrac{1}{2}\left(\tfrac{b^2}{f_1}+f_1\right)\sin\alpha - \tfrac{d_p}{2}\sin\alpha, \\ y_2 &= \tfrac{1}{2}\left(\tfrac{b^2}{f_1}+f_1\right)\cos\alpha - \tfrac{1}{2}\left(\tfrac{b^2}{f_1}-f_1\right) + \tfrac{d_p}{2}\cos\alpha. \end{aligned} \tag{A7}$$

Therefore,

$$\begin{aligned} L &= \frac{|\tan\alpha\cdot b - 0|}{\sqrt{1+\tan^2\alpha}} + \frac{|\tan\alpha\cdot x_0 - y_0|}{\sqrt{1+\tan^2\alpha}} \\ &= b\sin\alpha + \frac{1}{2}\left(\frac{b^2}{f_1}+f_1\right) - \frac{1}{2}\left(\frac{b^2}{f_1}-f_1\right)\cos\alpha. \end{aligned} \tag{A8}$$

A.3. Configuration (c): $\theta > \pi/2$ and $\pi-\theta \leqslant \alpha \leqslant \pi/2$ [or equivalently $1 \leqslant (1+\cos\alpha)/\sin\alpha < f_1/b$]

In this third case, the tangent contact points A and B are located at

$$\begin{aligned} x' &= \tfrac{1}{2}\left(\tfrac{b^2}{f_1}+f_1\right)\sin\alpha, \\ y' &= -\tfrac{1}{2}\left(\tfrac{b^2}{f_1}+f_1\right)\cos\alpha - \tfrac{1}{2}\left(\tfrac{b^2}{f_1}-f_1\right), \end{aligned} \tag{A9}$$

$$x_0 = -\tfrac{1}{2}\left(\tfrac{b^2}{f_1}+f_1\right)\sin\alpha,$$
$$y_0 = \tfrac{1}{2}\left(\tfrac{b^2}{f_1}+f_1\right)\cos\alpha - \tfrac{1}{2}\left(\tfrac{b^2}{f_1}-f_1\right). \quad \text{(A10)}$$

The center coordinates of the particles just touching the fiber are given as

$$x_1 = \tfrac{1}{2}\left(\tfrac{b^2}{f_1}+f_1\right)\sin\alpha + \tfrac{d_p}{2}\sin\alpha,$$
$$y_1 = -\tfrac{1}{2}\left(\tfrac{b^2}{f_1}+f_1\right)\cos\alpha - \tfrac{1}{2}\left(\tfrac{b^2}{f_1}-f_1\right) - \tfrac{d_p}{2}\cos\alpha. \quad \text{(A11)}$$

$$x_2 = -\tfrac{1}{2}\left(\tfrac{b^2}{f_1}+f_1\right)\sin\alpha - \tfrac{d_p}{2}\sin\alpha,$$
$$y_2 = \tfrac{1}{2}\left(\tfrac{b^2}{f_1}+f_1\right)\cos\alpha - \tfrac{1}{2}\left(\tfrac{b^2}{f_1}-f_1\right) + \tfrac{d_p}{2}\cos\alpha. \quad \text{(A12)}$$

Therefore, L becomes

$$L = \frac{|\tan\alpha\cdot x' - y'|}{\sqrt{1+\tan^2\alpha}} + \frac{|\tan\alpha\cdot x_0 - y_0|}{\sqrt{1+\tan^2\alpha}} = \left(\frac{b^2}{f_1}+f_1\right) = 2R. \quad \text{(A13)}$$

Next, we formulate the method for evaluating the distance between the two limiting streamlines, L_∞. We first note that the streamlines that pass through the point $C\,(x_1, y_1)$ and $D\,(x_2, y_2)$ are straight lines *at infinity* with a slope tan(α), namely

$$L_i : y_{i\infty} = x_{i\infty}\tan\alpha + K_i (i = 1,2). \quad \text{(A14)}$$

where K_i is the intercept and ($x_{i\infty}$, $y_{i\infty}$) is a point located on the streamline at the infinity. The distance between lines L_1 and L_2 can be written as

$$L_\infty = |(K_1 - K_2)\cos\alpha| = |(y_{1\infty}\cos\alpha - x_{1\infty}\sin\alpha) - (y_{2\infty}\cos\alpha - x_{2\infty}\sin\alpha)|. \quad \text{(A15)}$$

The streamfunction at point ($x_{i\infty}$, $y_{i\infty}$) takes the same value as that passing the point (x_i, y_i), namely,

$$\psi(x_{i\infty}, y_{i\infty}) = \psi(x_i, y_i). \quad \text{(A16)}$$

Since (ξ, η). $\xi_{i\infty} = 2x_{i\infty}$, $\eta_{i\infty} = 2y_{i\infty}$, then it follows from [Eq. (10)]

$$\frac{\psi(x_{i\infty},y_{i\infty})}{bV_\infty} = \frac{1}{2}\left[-\frac{2x_{i\infty}}{b}\sin\alpha + \left(\frac{2y_{i\infty}-f_1}{b}\right)\cos\alpha\right]\left[1+\frac{1+\left(\frac{f_1}{b}\right)^2}{\left(\frac{2x_{i\infty}}{b}\right)^2+\left(\frac{2y_{i\infty}-f_1}{b}\right)^2}\right] \approx \frac{1}{2}\left[-\frac{2x_{i\infty}}{b}\sin\alpha + \left(\frac{2y_{i\infty}-f_1}{b}\right)\cos\alpha\right]. \quad \text{(A17)}$$

Therefore, the coordination ($x_{i\infty}$, $y_{i\infty}$) can be obtained through (x_i, y_i) as

$$\frac{y_{i\infty}}{b}\cos\alpha - \frac{x_{i\infty}}{b}\sin\alpha = \frac{\psi(x_i,y_i)}{bV_\infty} + \frac{1}{2}\frac{f_1}{b}\cos\alpha. \quad \text{(A18)}$$

Then L_∞ can be determined as

$$\frac{L_\infty}{b} = \left|\frac{\psi(x_1,y_1)}{bV_\infty} - \frac{\psi(x_2,y_2)}{bV_\infty}\right| = \frac{1}{2}\left|\sum_{i=1,2}(-1)^i\left[\frac{\eta_i - f_1}{b}\cos\alpha - \frac{\xi_i}{b}\sin\alpha\right]\left(1-\frac{1+\left(\frac{f_1}{b}\right)^2}{\left(\frac{\xi_i}{b}\right)^2+\left(\frac{\eta_i}{b}-\frac{f_1}{b}\right)^2}\right)\right|. \quad \text{(A19)}$$

where the coordinates on the ζ (ξ, η) plane can be obtained based on the coordinates on the z(x, y) plane as

$$\xi_i = x_i \pm \sqrt{\frac{(x_i^2-y_i^2-b^2)+\sqrt{\left(x_i^2-y_i^2-b^2\right)^2+4x_i^2y_i^2}}{2}},$$
$$\eta_i = y_i \pm \sqrt{\frac{-(x_i^2-y_i^2-b^2)+\sqrt{\left(x_i^2-y_i^2-b^2\right)^2+4x_i^2y_i^2}}{2}}. \quad \text{(A20)}$$

Finally, the interception efficiency for different configurations becomes

Configuration (a): f1/b ⩽ (1-cos α)/sin α ⩽ 1

$$\eta_R = \frac{L_\infty}{L+d_p} = \frac{1}{2} \times \frac{\left|\sum_{i=1,2}(-1)^i\left[\frac{\eta_i-f_1}{b}\cos\alpha - \frac{\xi_i}{b}\sin\alpha\right]\left(1-\frac{1+\left(\frac{f_1}{b}\right)^2}{\left(\frac{\xi_i}{b}\right)^2+\left(\frac{\eta_i}{b}-\frac{f_1}{b}\right)^2}\right)\right|}{2\sin\alpha + \frac{d_p}{b}}. \quad \text{(A21a)}$$

Configuration (b): (1-cos α)/sin α⩽ f1/b ⩽ (1+cos α)/sin α

$$\eta_R = \frac{L_\infty}{L+d_p} = \frac{1}{2} \times \frac{\left|\sum_{i=1,2}(-1)^i\left[\frac{\eta_i-f_1}{b}\cos\alpha - \frac{\xi_i}{b}\sin\alpha\right]\left(1-\frac{1+\left(\frac{f_1}{b}\right)^2}{\left(\frac{\xi_i}{b}\right)^2+\left(\frac{\eta_i}{b}-\frac{f_1}{b}\right)^2}\right)\right|}{\sin\alpha + \frac{1}{2}\left[\left(\frac{b}{f_1}+\frac{f_1}{b}\right) - \left(\frac{b}{f_1}-\frac{f_1}{b}\right)\cos\alpha\right] + \frac{d_p}{b}}. \quad \text{(A21b)}$$

Configuration (c): 1 ⩽ (1+cos α)/sin α < f1/b

$$\eta_R = \frac{L_\infty}{L+d_p} = \frac{1}{2} \times \frac{\left|\sum_{i=1,2}(-1)^i\left[\frac{\eta_i-f_1}{b}\cos\alpha - \frac{\xi_i}{b}\sin\alpha\right]\left(1-\frac{1+\left(\frac{f_1}{b}\right)^2}{\left(\frac{\xi_i}{b}\right)^2+\left(\frac{\eta_i}{b}-\frac{f_1}{b}\right)^2}\right)\right|}{\left(\frac{b}{f_1}+\frac{f_1}{b}\right) + \frac{d_p}{b}}. \quad \text{(A21c)}$$

References

[1] Davies CN. Air filtration. London: Academic; 1973.
[2] Fardi B, Liu BYH. Flow field and pressure drop of filters with rectangular fibers. Aerosol Sci Technol 1992;17:36–44.
[3] Fardi B, Liu BYH. Efficiency of fibrous filters with rectangular fibers. Aerosol Sci Technol 1992;17:45–8.
[4] Fotovati S, Tafreshi HV, Pourdeyhimi B. Influence of fiber orientation distribution on performance of aerosol filtration media. Chem Eng Sci 2010;65:5285–93.
[5] Hinds WC. Aerosol technology: properties, behavior, and measurement of airborne particles. New York: Wiley-Interscience; 1999.
[6] Kim SC, Bao L, Okuyama K, Shimada M, Niinuma H. Filtration efficiency of a fibrous filter for nanoparticles. J Nanopart Res 2006;8:215–21.
[7] Landau LD, Lifshitz EM. Fluid mechanics. Oxford: Pergamon; 1959.
[8] Lee KW, Liu BYH. Theoretical study of aerosol filtration by fibrous filters. Aerosol Sci Technol 1982;2:147–61.
[9] Lee KW, Liu BYH. Experimental study of aerosol filtration by fibrous filters. Aerosol Sci Technol 1981;1:35–46.
[10] Lin JZ, Shi X, You ZJ. Effects of the aspect ratio on the sedimentation of a fiber in Newtonian fluids. J Aerosol Sci 2003;34:909–21.
[11] Moldavsky L, Fichman M, Gutfinger C. Enhancing the performance of fibrous filters by means of acoustic waves. J Aerosol Sci 2006;37:528–39.
[12] Ouyang M, Liu BYH. Analytical solution of flow field and pressure drop for filters with rectangular fibers. J Aerosol Sci 1998;29:187–96.

[13] Shamsuddin I, Douglas PL. Inertial impaction of aerosol particles on cylinders at intermediate and high Reynolds numbers. Chem Eng Sci 1989;44:81–99.
[14] Tahir MA, Tafreshi HV. Influence of fiber orientation on the transverse permeability of fibrous media. Phys Fluids 2009;21:083604.
[15] Ushe Z. The effect of different shaped cross-sectional microfibers on filtration. In: Leung WW, editor. Advances in filtration and separation technology, vol. 7. Kingwood: American Filtration Society; 1993. p. 146–7.
[16] Viswanathan S. An improved single droplet collection efficiency for the intermediate flow regime. Part Sci Technol 1998;16:215–27.
[17] Wang CS. Electrostatic forces in fibrous filters—a review. Powder Technol 2001;118:166–70.
[18] Wang HC. Theoretical adhesion efficiency for particles impacting a cylinder at high Reynolds number. J Aerosol Sci 1986;17:827–37.
[19] Wang HC, Kasper G. Filtration efficiency of nanometer-size aerosol particles. J Aerosol Sci 1991;22:31–41.
[20] Wang WX, Xie ML, Wang LP. An exact solution of interception efficiency over an elliptical fiber collector. Aerosol Sci Technol 2012;46:843–51.
[21] Wang WX, He Q, Chen N, Zhou Y, Xie ML. A solution for potential flow over an arc fiber. Thermal Sci 2012;16:1564–8.
[22] Watson JHP. Magnetic filtration. J Appl Phys 1973;44:4209–13.
[23] Yu MZ, Lin JZ, Chan TL. A new moment method for solving the coagulation equation for particles in Brownian motion. Aerosol Sci Technol 2008;42:705–13.
[24] Yuan H, Shapiro A, You ZJ, Badalyan A. Estimating filtration coefficients for straining from percolation and random walk theories. Chem Eng J 2012;210:63–73.
[25] Yuan H, You ZJ, Shapiro A, Bedrikovetsky P. Improved population balance model for straining-dominant deep bed filtration using network calculations. Chem Eng J 2013;226:227–37.